

Personally Natural Perception and Interaction in Mixed Reality

Meng Ma

November 16, 2015
Version: 0.0



Technische Universität München

Fakultät für Informatik

Lehrstuhl für Informatikanwendungen in der Medizin & Augmented Reality

Personally Natural Perception and Interaction in Mixed Reality

Meng Ma

Vollständiger Abdruck der von der Fakultät für Informatik der Technischen Universität München zur Erlangung des akademischen Grades eines

Doktors der Naturwissenschaften (Dr. rer. nat.)

genehmigten Dissertation.

Vorsitzende(r): ...
...

Prüfer der Dissertation: Prof. Nassir Navab, Ph.D.
Technische Universität München
Computer Aided Medical Procedures

[Prof. Dr.-Ing. Bernhard Preim]
Otto-von-Guericke-Universität
Institut für Simulation und Graphik

Die Dissertation wurde am bei der Technischen Universität München eingereicht und durch die Fakultät für Informatik am angenommen.

Meng Ma

Personally Natural Perception and Interaction in Mixed Reality

Dissertation, November 16, 2015

Reviewers: Prof. Nassir Navab, Ph.D. and **[Prof. Dr.-Ing. Bernhard Preim]**

Supervisors: Prof. Nassir Navab and Dr. Maximilian Baust

Technische Universität München

Fakultät für Informatik

Lehrstuhl für Informatikanwendungen in der Medizin & Augmented Reality

Boltzmannstraße 3

85748 and Garching bei München

Abstract

The continuous advances in the field of medical imaging constantly provide clinicians with new technology promising to facilitate diagnosis, interventions and therapies and improve their outcome. Inherent with this progress is that the amount of available data, its resolution and quality is **[heavily?]** increasing. However, such improvements are only of actual use if the data can be adequately presented to the clinician. Thus, visual computing in medicine is an important field of research. This thesis focuses on the development of such techniques specifically designed for medical ultrasound. One of the key strengths of ultrasound is its real-time capability allowing the clinician to interactively examine the patient's anatomy given the visual feedback while manipulating the ultrasound transducer. Therefore, the methods for advanced ultrasound image processing and visualization presented in this thesis are designed to ensure maintaining this interactivity.

At first, techniques for improved 2D B-mode ultrasound visualization are presented, where the observer is provided with real-time feedback on the uncertainty present in the image. Therefore, in a first step, the necessary information is generated through the computation of ultrasound Confidence Maps estimating per-pixel uncertainty information with respect to the ultrasound signal attenuation. While their original formulation has been proven to improve tasks such as image registration and segmentation, their valuable information has never been directly exposed to the clinician. Therefore, a real-time capable extension in form of an incremental solver scheme is presented and shown to yield precise results for visualization applications. The uncertainty information is eventually fused with the original B-mode images using three carefully chosen visualization schemes. Their benefit has been shown for both educational and clinical applications.

The second part of this thesis' contributions targets improved 3D ultrasound visualization. In order to generate high-quality 3D volumes from tracked ultrasound sweeps, first an incremental compounding scheme is presented, which combines orientation-driven correlation terms and the aforementioned Confidence Maps in an information fusion approach. The subsequent visualization of such ultrasound volumes is a particularly challenging task due to the special nature of B-mode intensities. Therefore, a novel classification concept in the form of point predicates is presented, which seamlessly integrates into the standard direct volume rendering pipeline. In conjunction with the proposed predicate histogram as intuitive user interface, this technique allows for much more meaningful visualization and facilitates the understanding of the data for the observer.

Acknowledgments

Performing a PhD is a one-of-a-kind experience and while being in the process usually everybody has to struggle with a similar set of issues. At the same time, certainly every PhD process is unique and everybody copes with the upcoming challenges differently. Coming to CAMP as kind of an *outsider* (in the sense of both coming from a different university and city - some might even say country - as well as focusing on a related but entirely different topic than the rest of the chair) **[erschweren the initial orientation?]**.

At first, I would like thank Prof. Navab and express my **[deepest gratitude?]** to him. In particular retrospectively, I appreciate the incredible amount of freedom he provided me for my work and his constant trust in my work.

Secondly, **[special honor goes to?]** my sister Marion who, recently successfully pursuing her own PhD, acted as kind of mentor for me during the last four years. The incredible value of our talks and...

Furthermore, I would like to thank Athanasios Karamalis, Benjamin Frisch, Christoph Hennersperger and Max Baust for their incredibly valuable support as (somewhat) senior colleagues. Even if it sometimes might only have been an open ear or a small hint, I feel that your constant encouragement to pursue my own ideas significantly contributed to my success. At this place I would also like to mention Timo Ropinski whose excellent lectures and lab course back in Münster actually raised my interest in medical visualization and thus made this work **[even/yet?]** possible.

Finally, I want to express my gratitude to my family and friends. I am personally not a friend of trying to enumerate all of them individually at such a place in order to thank them but try to always express my appreciation and gratitude directly at the **[appropriate?]** occasions.

Contents

I Methodology	1
1 Uncertainty Visualization for 2D Ultrasound	3
1.1 Uncertainty in Health Care and Medical Visualization	3
1.2 Clinical Significance and Application	5
1.3 Selection of Visual Variables	6
1.4 Visualization Schemes	7
1.4.1 Uncertainty as Color Overlay	7
1.4.2 Uncertainty Mapping to Chroma	9
1.4.3 Uncertainty Mapping to Fuzziness	10
1.5 Results and Evaluation	11
1.5.1 User Study with Ultrasound Novices	11
1.5.2 User Study with Ultrasound Experts	13
1.6 Conclusion	14
2 Advanced Ultrasound Compounding	15
2.1 Related Work	15
2.2 Correlation Terms for Tracked Ultrasound Sweeps	18
2.3 Orientation-driven Inter-frame Registration of Ultrasound Sweeps	19
2.4 An Information-fusion Approach to Ultrasound Compounding	20
2.4.1 Clustering of Ultrasound Sweeps by Direction	21
2.4.2 Compounding of each Cluster	22
2.4.3 Uncertainty-based Fusion of the Compounded Clusters	22
2.5 Incremental Compounding System	23
2.5.1 Incremental Compounding Pipeline	23
2.5.2 Real-time Implementation	23
2.6 Results and Evaluation	24
2.6.1 Parameter Evaluation	24
2.6.2 Reconstruction Accuracy	25
2.6.3 Reconstruction Quality	25
2.6.4 System Performance	27
2.7 Conclusion	28
Bibliography	31

Part I

Methodology

Uncertainty Visualization for 2D Ultrasound

Though there are many advantages of ultrasound imaging, such as being rather low-cost and real-time capable, the correct interpretation of B-mode images is a non-trivial task that requires a large amount of experience and training. Even ultrasound experts sometimes struggle in performing an ultrasound-based diagnosis due to the presence of many different kinds of artifacts and it's non-homogeneous distribution of uncertainty. In this chapter we present novel visualization techniques that augment the B-mode images with uncertainty information in real-time in order to support both ultrasound novices and expert users in gaining a better understanding of ultrasound. Therefore, we build upon the previously introduced method of real-time confidence estimation for B-mode ultrasound images (cf. Chapter ??) and interpret these Confidence Maps as per-pixel uncertainty information, which we expose to the user using perceptual visualization techniques. After a review on general uncertainty visualization techniques for medical applications, we discuss the clinical significance of our proposed system. In total, we present three different visualization schemes for both educational and clinical applications and motivate the selection of visual variables to depict uncertainty in B-mode ultrasound images. An extensive evaluation conducted with both ultrasound novices and expert clinicians demonstrates the usefulness of our techniques. Parts of this work have been published in [\[citation needed\]](#).

1.1 Uncertainty in Health Care and Medical Visualization

When [\[having?\]](#) a comprehensive look at health care, the concept of uncertainty is ubiquitous throughout all levels. However, since clinicians have been trained to make decisions and provide their patients with answers, many of them struggle to admit that their work is based on a plethora of input factors, each inducing an individual level of uncertainty, and thus their eventual findings rather represent the most likely interpretation than the [\[absolute truth?\]](#).

Han et al. investigate the different concepts and appearances of uncertainty in general health care using cancer treatment as example and derive a conceptual taxonomy in [6]. They point out that a coherent concept of uncertainty in health care is missing and that multiple meanings and interpretations of that term are present, which are not necessarily distinguished from each other. They conclude that uncertainty is actually a threefold concept which can originate either through probability, ambiguity or complexity with issues ranging from disease-centered to patient-centered ones.

While the paper of Han et al. analyzes the problem from the clinical perspective, Ristovski et al. focus on the various technical aspects and investigate the presence of uncertainty in

medical visualization [21]. As introduced in Section ??, the visualization pipeline ranges from the initial acquisition of data, over several data processing steps to the final rendering output. Though each of these steps is subject to an individual level of uncertainty, the final rendering often shows the data as if it were the only possible truth. However, it requires appropriate visualization to make the amount of uncertainty assessable to the clinician and thereby propagate the information back correctly to the clinical perspective as it was previously presented by Han et al. For instance, Lundström et al. point out that a suboptimal setup of a transfer function during rendering can lead to a false classification of stenosis [11].

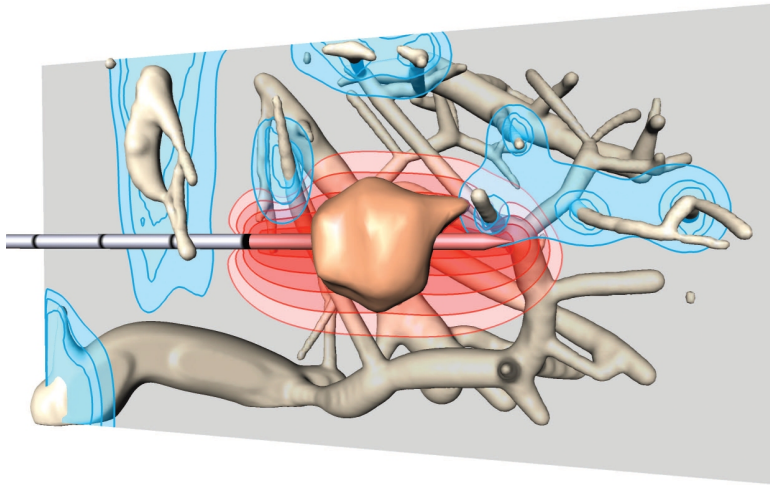


Fig. 1.1 Uncertainty visualization of radio-frequency ablation zones as proposed by Rieder et al. [20].

The special setup in which medical visualization is used and its resulting requirements make it difficult to apply techniques from other domains, such as [15, 17], even though they use very similar data. This may be one of the reasons why the body of literature on medical uncertainty visualization is rather shallow and the individual works are very application- and task-specific. One such example is the uncertainty visualization technique of Rieder et al. proposed in the context of percutaneous radio-frequency ablation. For this application, precise planning of the applicator placement is crucial in order to ensure that the malignant tissue is destroyed completely (cf. Figure 1.1). Their work is particularly noteworthy as they use their visualization for the optimization of a seven-dimensional optimization problem (five degrees of freedom for the placement of each needle plus two free simulation parameters) in three-dimensional space [20]. Another similar approach is the work of Brecheisen et al. exploring the parameter sensitivity in fiber tracking algorithms for DTI data [3]. Both techniques rely on interactive exploration by the user in order to cover the available parameter space.

One example of providing feedback on the uncertainty present in medical imaging algorithms is the work of Praßni et al. They propose a guided probabilistic volume segmentation technique for which they visualize the resulting uncertainty distribution using iso-lines and opacity modulation (cf. Figure 1.2). As mentioned previously, it is crucial to expose information on the result quality to the clinician, since ultimately they have to decide on diagnosis and treatment. The recent progress on ensemble visualizations [7, 14, 19] could be influential for further progress in this direction. In the medical domain such techniques can for instance

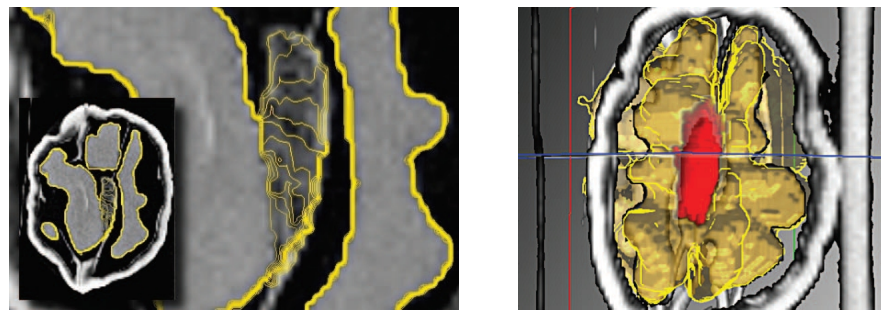


Fig. 1.2 Uncertainty visualization of segmentation algorithm results as proposed by Prassni et al. [18].

be used to visualize the results of large random studies on medical imaging algorithms and thereby make them more accessible.

1.2 Clinical Significance and Application

Compared to other anatomical medical imaging modalities such as CT or MRI, medical ultrasound exhibits several benefits, such as being comparatively cheap, portable and real-time capable. It is therefore widely used in today's clinical practice, for instance for abdominal, pediatric, head and general vascular applications [13]. However, acquiring a good image (e.g. in terms of high diagnostic value) is a non-trivial task due to the highly complex ultrasound image formation process (cf. Section ??). It is influenced by various physical imaging parameters such as frequency, focus, and depth, as well as by external factors such as probe positioning, probe pressure, patient positioning and patient breathing cycle [1], and can yield a wide range of image artifacts [23]. Furthermore, some target anatomies can not be directly reached but need to be scanned by circumventing strong reflectors such as bones, which prevent the acquisition of images underneath. A classic example of such an anatomy are the kidneys, which can not be scanned from the back as they are then in the acoustic shadow of the spine reflecting almost all ultrasound waves. Instead, sonographers perform kidney ultrasound through the abdomen, usually using the liver as an acoustic window since it has the best transmission properties of the surrounding anatomy.

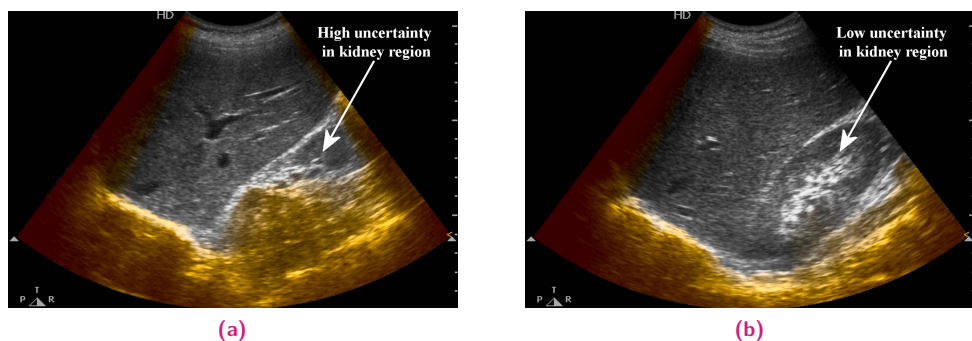


Fig. 1.3 Kidney ultrasound using the liver as acoustic window with applied uncertainty visualization using chroma as visual variables (cf. Section 1.4). A slight repositioning of the transducer results in a considerable increase of confidence in image (b) compared to (a).

Sonographers need to be aware of all these caveats of ultrasound imaging in order to correctly understand the image. In particular medical trainees and ultrasound novices have difficulties in getting the right image needed for their clinical objectives since traditional ultrasound imaging does not provide a direct qualitative feedback on the image quality. Already a slight repositioning of the transducer can yield a significantly better acoustic window and thus improve the image for the target anatomy (cf. Figure 1.3). Thus, training is an important aspect for medical students when learning ultrasound [5]. In particular in trauma applications, where time is critical, the surgeon has to determine possible fractures and lesions as quickly as possible and has a minimal margin for error [10]. With this motivation in mind, we developed our work with the aim to support both medical students in learning sonography as well as expert clinicians for a more quick and intuitive interpretation of ultrasound images by providing an interactive feedback on the image quality and uncertainty distribution.

1.3 Selection of Visual Variables

Essentially, we target two different applications with our work: On the one hand, we are convinced that exposing uncertainty information to ultrasound novices and trainees helps them to better understand the complex ultrasound image formation process. At the same time, we also expect expert sonographers to benefit from uncertainty visualization as the additional information may improve the diagnostic value of the image. Regarding these two target applications, we yield the following requirements for ultrasound uncertainty visualization schemes.

- The uncertainty information should be fused directly into the original B-mode sequence. Thus, both the spatial and the temporal domain are fixed.
- The primary information in the uncertainty maps are not the exact per-pixel uncertainty values but the distribution of the uncertainty with respect to the anatomy (cf. Section ??).
- For educational applications, the uncertainty distribution in the image should be easily and intuitively perceivable. Even small changes in the uncertainty distribution should be clearly observable when repositioning the ultrasound probe in order to maximize the learning effect.
- For clinical applications, the diagnostic information in the B-mode image must not be impaired. Thus, the original image intensities should be preserved as good as possible and no image regions should be occluded.

Given these requirements for our uncertainty visualization, the number of viable visual variables for depicting the uncertainty information is limited.

One traditional technique is the usage of glyphs for depicting uncertainty, with error bars in 1D visualization being the classic example. Glyphs have the advantage of offering a large number of visual variables that can be used to alter their appearance. For instance, MacEachren et al. evaluate 11 different mappings of uncertainty to point glyphs [12]. Glyphs excel in depicting uncertainty when used in sparse layouts allowing the observer to individually focus on single glyphs in order to read their information. However, this does not work well for our application where the goal is to visualize the distribution of a dense 2D scalar field. Although dense

glyph fields have also been successfully used for depicting global information [9, 2], we do not consider them for our work since early experiments did not show promising results. The work of Sanyal et al. supports this fact as their experiments showed that in many uncertainty related tasks on 2D data sets the different glyph mappings perform significantly worse than surface color mapping [22]. Furthermore, adding glyphs to the B-mode image would occlude the original ultrasound image, which is undesirable for clinical applications.

One intriguing approach is to extend the 2D data to the third dimension and map uncertainty to the Z axis in a 3D rendering [4, 8]. While this may be a valid method for applications such as geospatial visualization, it can not be applied to our use case since, due to the 2D projection of a 3D scene, it requires the user to interact with the camera to get the full information. Furthermore, as mentioned above, the spatial domain of our visualization is fixed as clinicians expect a 2D image when performing 2D B-mode ultrasound.

Another approach is to exploit the spatial domain for depicting uncertainty, for instance through animations, animated jittering or probabilistic animation [4, 11]. However, since we are working with real-time ultrasound sequences, the temporal domain is fixed and such approaches are not applicable. *[extend the last two paragraphs/this section]*

1.4 Visualization Schemes

Given these considerations and the particular requirements of our intended uncertainty visualization, we selected the visual variables of color and texture. They both do not affect the spatial and temporal image domain and are very powerful and intuitive for expressing general uncertainty [12]. In total, we propose three different uncertainty mapping techniques for the two applications, which we will discuss in detail in the following sections. Since both the B-mode image and the uncertainty map are in the same image domain, no coordinate transformation is necessary and the mapping techniques are focused on the optical properties.

As illustrated in Figure 1.4, all proposed mapping schemes start with the original B-mode ultrasound image I , for which we compute the corresponding Confidence Map. We assume it to be inversely related to the amount of uncertainty in the image, more precisely to its facets of accuracy, precision and credibility. Thus, we obtain the per-pixel uncertainty information U by applying a direct inverse linear mapping

$$U(x) := 1 - CM(x), \quad (1.1)$$

where $CM(x) \in [0, 1]$ is the confidence map value at pixel x in the image domain.

1.4.1 Uncertainty as Color Overlay

For educational applications, the focus of the visualization should be on the uncertainty information and even small changes in the distribution should be clearly distinguishable by the observer. At the same time, the corresponding ultrasound B-mode image should be shown as anatomical reference in order to allow for an understanding of the connection between

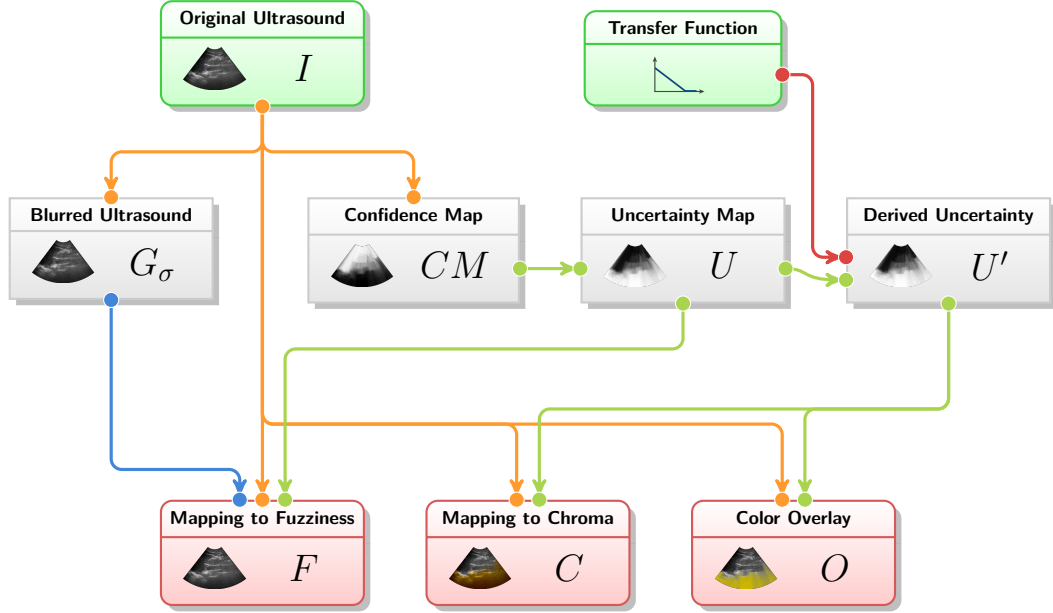


Fig. 1.4 Schematic diagram of the different proposed uncertainty visualization schemes. Given the original B-mode ultrasound image I , we compute its Confidence Map CM and a Gaussian blurred version G_σ . The uncertainty map U is derived from CM by inverse linear mapping (cf. Equation 1.1). For the color overlay and the uncertainty mapping to chroma, we compute a derived uncertainty measure U' using a transfer function. Finally, the uncertainty information is fused into the original ultrasound image using one of the three visualization schemes.

image features and their effects on the uncertainty. Therefore, we combine the visual variables of hue and value in our proposed color overlay scheme (cf. Figure 1.4). Compared to the other presented mapping schemes, the combination of the two visual variables makes even subtle changes of uncertainty visible to the observer. We deem this an important feature to teach ultrasound novices the caveats of the ultrasound image formation process.

As previously introduced, for each pixel x , let $U(x)$ be its uncertainty value and $I(x)$ be its original B-mode intensity. Since the color overlay is a very obtrusive mapping scheme, we use a transfer function to apply a thresholding to the uncertainty measure and define the derived uncertainty as $U'(x) := \max(0, 2U(x) - 1)$. Using this derived measure instead of the original $U(x)$ avoids overlaying regions of negligible uncertainty. We first generate the color overlay in HSV color space as

$$C(x)_{HSV} := (H, U'(x), V), \quad (1.2)$$

with constant hue $H \in [0, 1]$ and constant value $V \in [0, 1]$. We chose a bright orange color with $H = 0.15$ and $V = 0.8$ to avoid lowering the contrast to Doppler ultrasound utilizing the colors blue and red. In a second step, we linearly mix the color overlay transformed to RGB color space with the original B-mode to yield the final pixel color

$$O(x) := U'(x) \cdot C_{RGB}(x) + (1 - U'(x)) \cdot I(x). \quad (1.3)$$

Figure 1.5 shows the uncertainty color overlay applied to two different abdominal ultrasound images.

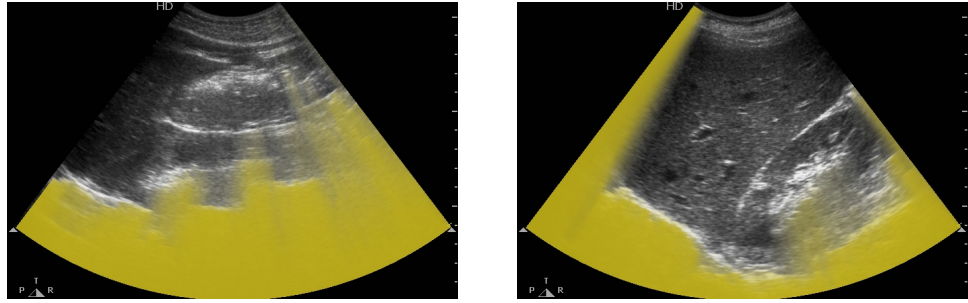


Fig. 1.5 Illustration of the color overlay mapping scheme. The high contrast yellow overlay allows for an [\[clear investigation?\]](#) of the signal loss effects in ultrasound.

Since the original B-mode intensities are altered in this mapping scheme, we propose to use it only for educational purposes to give ultrasound novices a better understanding of the image formation process, but do not consider it for clinical usage. Furthermore, the color overlay also partially occludes the original ultrasound intensities. Although image regions of low confidence may not be reliable enough for diagnosis, they still contain structural information, which can help the sonographer in navigating towards the correct anatomy and optimizing the acoustic window. Thus, hiding these parts completely is disadvantageous for clinical usage, which was later also confirmed by some candidates during our evaluation (cf. Section 1.5). Therefore, we additionally propose two alternative mapping schemes maintaining structural information also in highly unreliable regions.

1.4.2 Uncertainty Mapping to Chroma

For clinical applications, we propose additional uncertainty visualization schemes that maintain the structural information in the ultrasound B-mode image also in unreliable regions. Similar to the color overlay, uncertainty mapping to chroma also uses color to depict uncertainty but uses chroma as visual variable.

In order to preserve the original ultrasound image's diagnostic value, we need to ensure that the perceived intensity remains the same when augmenting the image with uncertainty information. Therefore, we perform the chroma modification in the perceptually uniform CIE $L^*C^*h^*$ color space, the polar coordinate derivative of the CIE $L^*a^*b^*$ color model [16].

As illustrated in Figure 1.4, we compute the derived uncertainty from the original Confidence Map as $U'(x) := \max\left(0, \frac{3U(x)}{2} - \frac{1}{2}\right)$ to again avoid coloring regions with negligible uncertainty. The final pixel color in $L^*C^*h^*$ space is given by

$$C(x)_{L^*C^*h^*} := (I(x)_{L^*}, U'(x), H), \quad (1.4)$$

where $I(x)_{L^*}$ is B-Mode intensity transformed to L^* space and $H = 0.23$ is a bright orange. Again, we chose bright orange as hue for depicting uncertainty to avoid lowering the contrast to Doppler ultrasound. Sample images are shown in Figure 1.6.

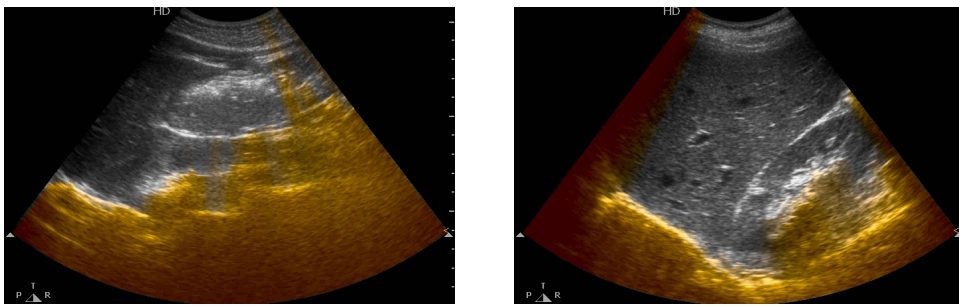


Fig. 1.6 Illustration of the chroma mapping scheme. Unreliable regions in the image are depicted with an orange overlay. Since the color transformation is applied in the perceptually uniform CIE L^{*}C^{*}h^{*} color space, the perceived pixel intensity is maintained.

1.4.3 Uncertainty Mapping to Fuzziness

Many clinicians prefer to look at gray scale ultrasound images as they have been trained to do so. Since texture is a very effective visual variable that keeps the spatial, temporal and color domain of the original image, we selected it as third visualization scheme for real-time B-mode ultrasound. More precisely, we use the visual cue of fuzziness to map the uncertainty information. Therefore, we fuse the ultrasound image with its uncertainty map such that regions of low uncertainty appear sharp and regions of high uncertainty appear fuzzy. As a matter of fact, according to MacEachren et al., this visual variable is also the most intuitive to represent uncertainty [12].

Our proposed uncertainty mapping to fuzziness combines a slight Gaussian blur of the original ultrasound image with its unsharp mask (subtraction of the blurred image from the original image). As illustrated in Figure 1.4 we compute the confidence map of the original image and apply Equation 1.1 to obtain the uncertainty value $U(x)$ for each pixel x . Since this is a diverging mapping scheme, where regions with high uncertainty will be blurred, and regions of low uncertainty will be sharpened, we can directly use $U(x)$ and do not need to compute a derived uncertainty measure. We compute a Gaussian filtered version of the original image and combine the two to yield the final pixel value $F(x)$ as

$$F(x) = U(x)G_\sigma(x) + ((1 - U(x)) \cdot (2I(x) - G_\sigma(x))), \quad (1.5)$$

where $I(x)$ is the original ultrasound intensity and $G_\sigma(x)$ the corresponding intensity in the Gaussian with parameter σ . We choose $\sigma = 2.5$ to limit the blurring to a tolerable amount but still yield the effect of perceived differences in fuzziness. An exemplary result can be seen in Figure 1.7.

It should be noted that this mapping scheme certainly alters the original B-mode image in a way that may reduce the amount of original information in regions of high uncertainty. However, discussions with clinicians showed that they nevertheless like uncertainty mapping to fuzziness and appreciate the intuitiveness of the visual variable. Our evaluation results in Section 1.5 underline this fact.

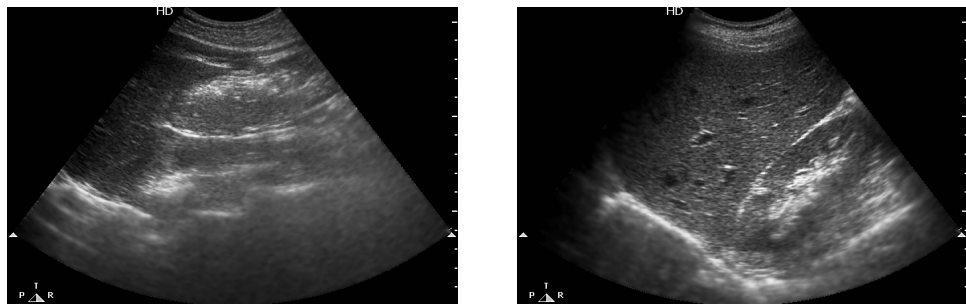


Fig. 1.7 Illustration of the fuzziness mapping scheme. Unreliable regions in the image are blurred while reliable regions are sharpened through unsharp masking. Especially in video sequences this provides a very strong perceptual cue for uncertainty while at the same time maintaining the ultrasound image in its original gray scale color domain.

1.5 Results and Evaluation

We performed the evaluation of the proposed methods independently for the two target applications. Therefore, we implemented a fully working reference system using an Ultrasonix RP (Analogic Corporation, Peabody, MA, USA) ultrasound device for the acquisition of images. Using OpenIGTLINK [25], we stream the ultrasound frames and imaging parameters to a standard workstation where our computation framework performs the necessary processing steps before eventually routing the fused image back to the ultrasound device's display. The processing pipeline is implemented in the CAMPVis framework [24] and entirely executed on the GPU using both CUDA (solving of Equation ??) and OpenGL/GLSL (all other processing steps) in order to achieve optimal performance. After acquiring the B-mode image, we perform a Gaussian filtering as well as a resampling. Gaussian filtering is required in order to remove high-frequency noise as well as to allow for our uncertainty mapping to fuzziness. We perform the downsampling to speed up the computation of the Confidence Maps and achieve better convergence (cf. Chapter ??). For our experiment setup we used a 0.5 scaling factor and a smoothing factor σ of 2.5. Finally, one of the discussed uncertainty visualization schemes is applied and the rectilinear B-mode image in polar coordinates is scan converted to Cartesian coordinates using the known probe geometry and dynamically queried imaging parameters.

1.5.1 User Study with Ultrasound Novices

In a first user study we evaluated the educational value of our proposed system. We equipped our ultrasound machine with an Ultrasonix C5-2/60 convex abdominal transducer and asked ultrasound novices to locate different structurally deep anatomies in a CIRS abdominal phantom while using our uncertainty visualization techniques. In total we interviewed 13 medical students, which all had very limited experience with ultrasound (average of 5.6 performed ultrasound examinations, minimum 0, maximum 20).

For a quantitative evaluation, we recorded the acquisitions and measured the time the users required to optimize the view on anatomical targets. After giving the participants some time to familiarize themselves with the phantom anatomy, we asked them to find an optimal view onto the vessel targets in the left and right kidney, as well as onto the portal vein. We then measured the required time to optimize the view for each visualization scheme by counting the number

	Left Kidney	Right Kidney	Portal Vein
	Average Time (seconds)		
Original B-Mode	6.73 ± 4.3	4.96 ± 1.6	4.78 ± 1.2
Color Overlay	4.74 ± 3.8	4.26 ± 1.5	3.30 ± 1.7
Chroma Mapping	4.19 ± 2.3	3.42 ± 1.8	3.44 ± 1.5
Fuzziness Mapping	3.49 ± 3.9	3.15 ± 0.7	2.67 ± 1.1

Tab. 1.1 Quantitative evaluation results of our user study with ultrasound novices. The table shows the average time (*seconds*) required to optimize the view on target anatomies (aggregated results from 9 of the 13 users, since not all acquisitions were complete). With enabled uncertainty visualization, the users managed to decide faster when they had a good view on the target anatomy than with the plain B-mode image.

of frames between the first frame where the target anatomy was in the field of view until the frame where the student defined the view as optimal in their personal opinion. To avoid biasing the results, we shuffled the order of the visualizations for each user. While the results in Table 1.1 show no significant differences between color overlay and chroma mapping, the time needed with fuzziness mapping is consistently lower (in average 0.79 seconds) than with the one of other two mapping schemes. Furthermore, the students performed significantly worse (in average 1.86 seconds longer) with only the original B-mode image compared to all of our proposed visualization schemes, which supports our idea that visualizing uncertainty helps the user in interactively assessing the quality of the acquired ultrasound image.

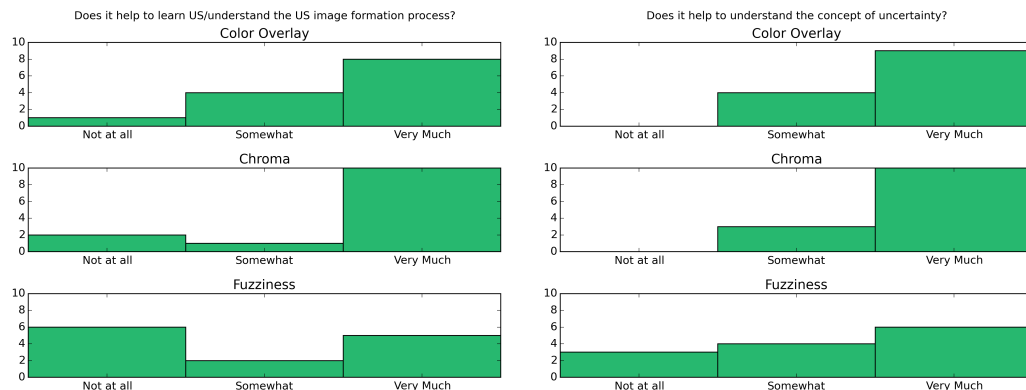


Fig. 1.8 User study results on the educational value of our technique to ultrasound novices. Almost all test subjects appreciate the added uncertainty visualization and confirm that it helps them with understanding the ultrasound image formation process and getting a better understanding of uncertainty in B-mode imaging.

After the experiment, the test subjects additionally answered a short questionnaire on different aspects of the presented visualization schemes. In the first set of questions we asked the students whether they generally appreciate the additional information presented to them, whether it helps them to better understand the ultrasound image formation process and whether it helps them with understanding the concept of uncertainty in B-mode images. The results (cf. Figure 1.8) indicate a general level of appreciation for our presented techniques, since especially the color overlay method got very positive results. In the second set of

questions the students were asked to assess the intuitiveness of the presented visualizations and whether our technique helps them in finding anatomical structures faster. As shown in Figure 1.9, ultrasound novices find the colorful visualizations much more intuitive than the fuzziness mapping. However, only a few students found the presented visualizations helpful to find target anatomies faster. Interestingly, fuzziness mapping yielded an overall worse response in the questionnaire, as many students considered this scheme as not helpful for diagnosis nor intuitive to read. This result is particularly interesting as it contradicts the quantitative results of Table 1.1.

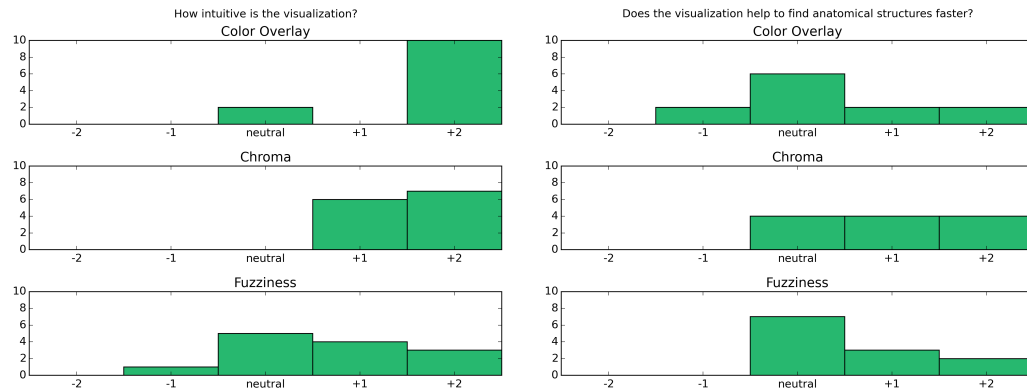


Fig. 1.9 User study results on the perception and clinical value for ultrasound novices on a 5-point Likert scale. While there is no clear favorite visualization scheme, a bias towards the colorful mappings is present. Furthermore, some students said that the added information helps them with finding target anatomical structures faster.

1.5.2 User Study with Ultrasound Experts

In a second user study, we presented our system to expert sonographers in order to evaluate the clinical significance of real-time ultrasound uncertainty visualization. Therefore we applied our visualization schemes to clinical data of abdominal ultrasound and presented the results to 7 experts (5 clinicians, 2 senior researchers). We presented them two patient abdominal ultrasound sequences of three different anatomies (liver, kidney, spleen) and asked them about perception, clinical value as well as whether our techniques assist in finding the optimal acoustic window. Since, for clinical usage, we do not want to hide information in the B-mode image, we evaluated only mapping to chroma and mapping to fuzziness.

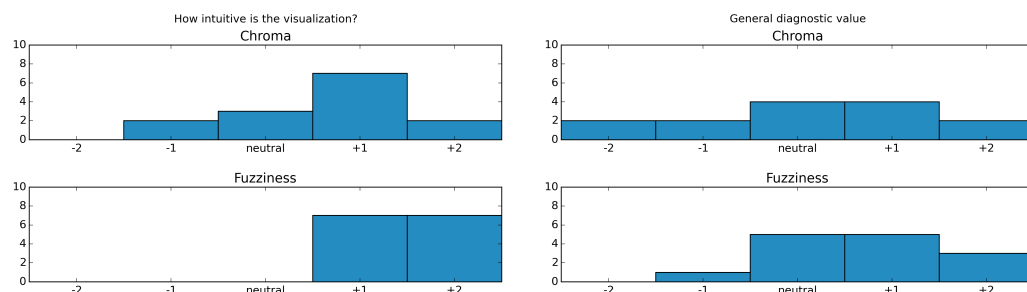


Fig. 1.10 Questionnaire results on expert sonographers' uncertainty perception. Each question was answered independently for the two different sequences. Therefore, there are 14 answers in total.

As shown in Figure 1.10, the expert sonographers clearly prefer mapping to fuzziness over mapping to chroma. The results on general diagnostic value are quite mixed. While there is a slight positive response for the gray scale fuzziness mapping, the chroma mapping performs rather bad in this regard. This discrepancy compared to ultrasound novices is probably due to the fact that experts got used to the monochrome appearance of B-mode ultrasound over the years. Thus, they prefer a visualization scheme that keeps the image in its original gray scale domain.

In addition to asking about the general diagnostic value, we also asked more specific questions regarding the clinical significance. Here, the study shows significant improvements compared to the default visualization in today's ultrasound devices (Table 1.2). The clinicians reported that seeing the amount of uncertainty dynamically adapting to the ultrasound view provides them with a very strong feedback on the image quality and its credibility. Here, 6 out of 7 stated that our uncertainty visualization helps with the correct interpretation of the images and also 6 out of 7 participants confirmed that the proposed real-time visualization schemes assists in optimizing the acoustic window. One clinician found that the computed Confidence Map was unexpected in one of the sequences and therefore confused him with the correct interpretation of the image. Nevertheless, he stated that the technique was helpful for optimizing the acoustic window. One other clinician confirmed the uncertainty visualization to be helpful for the correct interpretation but had doubts that it helps with optimizing the acoustic window.

	Yes	No
Helps with Correct Interpretation	86%	14%
Helps Optimizing Acoustic Window	86%	14%

Tab. 1.2 Results on expert sonographers evaluating the clinical value.

1.6 Conclusion

In this chapter we introduced a novel [\[paradigm?\]](#) to 2D ultrasound visualization. Instead of only showing the plain B-mode image, we augment it with additional uncertainty information based on the estimated per-pixel signal attenuation. Though different works have introduced the concept of uncertainty to ultrasound image processing, such information has never been exposed to the user.

To do so, we build upon the previously introduced technique of real-time uncertainty estimation (cf. Chapter ??) and fuse Confidence Maps with their original B-mode image. Targeting both educational and clinical applications, we present three individually designed visualization schemes. After implementing a fully working system, we ran two user studies [\[on/with?\]](#) both ultrasound novices and experts sonographers. The results clearly show the benefit of our technique for educational purposes as the added feedback on the signal attenuation helps students interactively learn how the ultrasound image formation process works. Also most clinicians value the additional information since it can help them with optimizing the acoustic window on target anatomies.

Advanced Ultrasound Compounding

The traditional imaging modalities used for musculoskeletal (MSK) applications are X-Ray, MRI and 2D B-mode ultrasound. Each of these exhibits its own advantages and drawbacks [vanhoenacker2007orthopedicImaging]: While being rather fast and low-cost, X-Ray uses ionizing radiation and shows only weak soft tissue contrast, and for instance can not resolve a tendon from its surroundings. MR images show an excellent resolution of the MSK anatomy, however their acquisition is rather slow and expensive, and the large footprint of the scanner often restricts the patient anatomy to be in a sub-optimal position for diagnosis. 2D B-mode ultrasound combines the advantages of X-Ray and MRI by being rather cheap, real-time capable and yielding high resolution images with good soft tissue contrast. However, the 2D imaging plane is mostly perpendicular to the skin surface so that some anatomies such as the tendons can only be imaged in cross sections and not in its full extent [Noble06, Noble11]. Ultrasound spatial compounding alleviates this drawback by reconstructing 3D volumes from 2D ultrasound sweeps. Traditional techniques usually require constant probe pressure or linear sweep trajectories to achieve good quality reconstructions. For applications such as MSK ultrasound however, these constraints do not hold since the anatomy is prone to deformation and exhibits high curvature surfaces.

In this paper, we introduce a novel orientation-driven framework for compounding 3D volumes from tracked 2D B-mode ultrasound sweeps. Using a set of orientation-driven correlation terms, we perform a complementary pressure compensation and then cluster the ultrasound frames into groups of homogeneous orientation. These groups of frames are then compounded individually and eventually fused into the final volume using an information fusion approach based on uncertainty. Thereby, our technique yields accurate and artifact-free 3D reconstructions also with challenging acquisition setups where the ultrasound sweeps exhibit pressure changes or curved trajectories - situations where traditional compounding methods often fail. Finally, we propose a novel incremental compounding scheme, which allows for interactively updating the reconstructed volume during the acquisition and can thus be used in real-time applications.

2.1 Related Work

Following Solberg et al.'s survey paper [Solberg07], one can classify ultrasound compounding techniques into three different approaches:

Early approaches were the *pixel-based* or *forward warping methods*, which traverse the pixels in each 2D ultrasound frame, project each pixel's location into the coordinate system of the target volume and write the pixel's intensity information into the initially empty corresponding

voxel. Pixel-based methods vary in the used averaging of multiple pixels contributing to a single voxel and in the employed hole filling of regions where the grid resolution is higher than the frame sampling rate of the ultrasound sweep. They are computationally rather cheap but their reconstruction quality is limited.

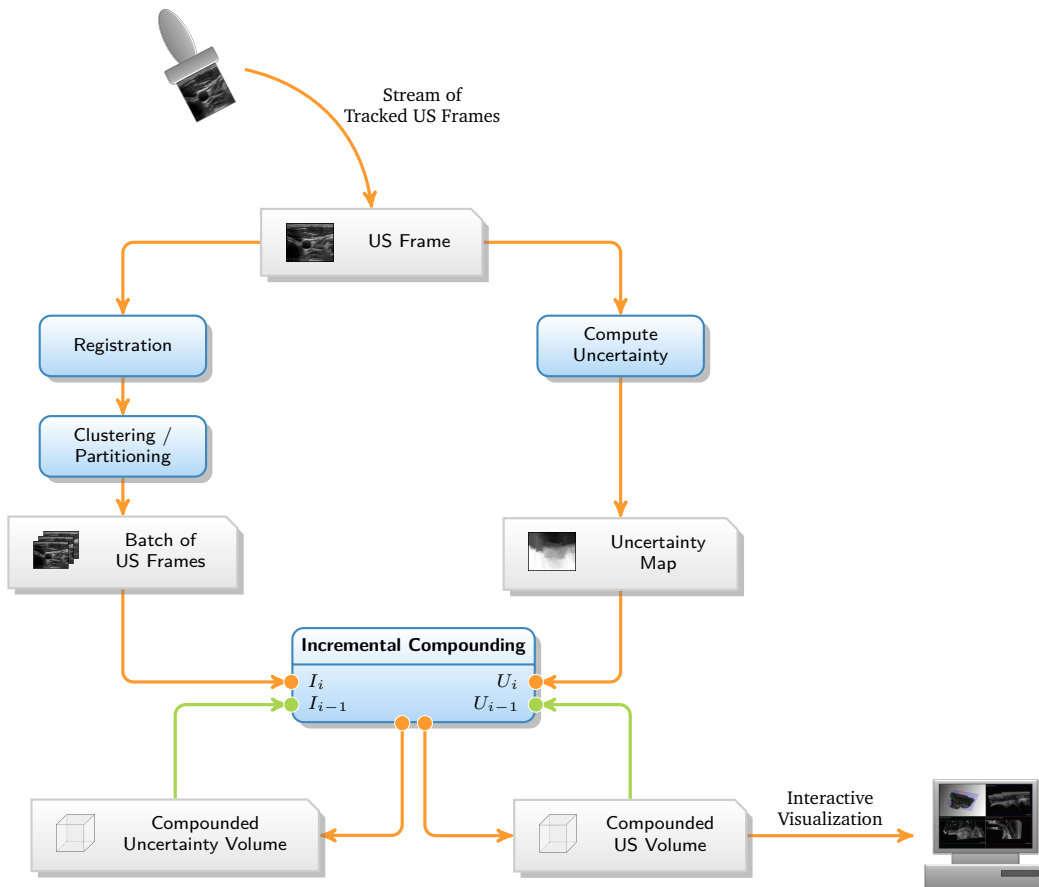


Fig. 2.1 Schematic diagram of the proposed incremental compounding technique. We acquire a constant stream of tracked ultrasound frames and compute the per-pixel uncertainty for each frame. We furthermore, perform the on-line inter-frame registration and partition the stream into small batches of homogeneous orientation. Our incremental compounding then continuously compounds the batches into the accumulated ultrasound intensity and uncertainty volume. After each incremental compounding step the interactive visualization can be updated.

Voxel-based methods such as [Coupe05, Wein06] use the inverse approach and are thus also referred to as *backward warping* methods. They traverse the voxel grid of the target volume and back-project their position into the pixel space of each ultrasound frame to lookup the image intensity. Since multiple pixels may contribute to the final voxel value, they employ a weighting function based on intensity and/or distance. Wein et al. show that voxel-based methods yield superior quality compared to pixel-based methods [Wein06]. Furthermore, backward warping algorithms are capable of reconstructing subsets of the target volume alone (e.g. a multi-planar reconstruction (MPR)), which offers a computational benefit over forward warping methods in such situations). However, their use in real-time interventional imaging is limited as their workflow requires to first acquire the whole sweep before the reconstruction process can start.

Finally, *function-based methods* estimate the coefficients for a set of locally supported basis functions to approximate the input data. These functions are then evaluated on the voxel grid to reconstruct the compounded volume [Rohling1999, Sanches2002, Klein12]. Function-based techniques can further be extended to more than three dimensions to reconstruct time-varying data such as 3D velocity fields with a flow profile from Doppler ultrasound [zettinig14]. While these methods yield 3D ultrasound reconstructions of very high quality, they are currently not feasible for interactive clinical practice due to their high computational costs. In terms of reconstruction quality, recently introduced tensor-based approaches yield results comparable to traditional spline-based methods, while at the same time offering a much lower computational complexity [Morozov11].

When browsing the scientific literature on this topic, one realizes that most works on ultrasound compounding make simplified assumptions on the input data and presume constraints such as constant probe pressure and/or constant motion of the ultrasound transducer along a linear path. However, since the ultrasound transducer has to be always in contact with the skin surface, these assumptions do not hold for applications where the anatomy exposes high curvatures, such as MSK. Here, the compounding algorithms do not only need to deal with the inherent probe pressure changes, but may also have inconsistent intensity information for the same reconstructed voxel due to overlapping image frames. Such overlapping frames pose a particular challenge, since ultrasound may yield different information (i.e. image intensities) for the same point within the anatomy if scanned from different perspectives or at different times. This is due to the dynamics and high complexity of the ultrasound image formation being dependent on incident angle, probe pressure and patient positioning [aldrich07usphysics]. Traditional, solely distance-based compounding methods do not resolve such ambiguities so that their reconstructions may show image artifacts and low continuity of the image, as well as have wrong image intensities due to performing averaging on opposing information.

To the best of our knowledge, there currently exist no work on explicitly resolving such ambiguities. The only method compensating for probe pressure changes are the works of Treece et al. who use an image-based non-rigid registration technique [Treece02]. By computing the line-wise maximum normalized correlation between two adjacent B-mode images and applying a monotonicity constraint, they estimate the deformation in depth introduced by the probe pressure. To avoid drift in the registration, they constrain the registration results to the tracking.

This work on real-time orientation-driven ultrasound compounding is an extension of our original approach as presented in [SchulteZub14] and contains the following main contributions:

- An updated framework of orientation-driven correlation terms with a more generalized and simpler distance-based term.
- Clustering the frames of a sweep by orientation to handle the view dependency of ultrasound.
- An information fusion approach to ultrasound compounding exploiting uncertainty information.

- An incremental ultrasound compounding scheme (cf. Fig. 2.1) that allows for interactive updates of the volume during the acquisition.
- An OpenGL-based GPU implementation of the incremental compounding scheme achieving real-time performance for clinically adequate resolutions.

We use our framework of correlation terms also for pressure compensation. However, this aspect is mostly of complementary nature and not intended to compete with the more elaborate method of Treece et al. [Treece02]. Instead, the goal of our compounding is to free clinicians from restrictive scanning protocols so that they can concentrate on which images they acquire instead of on how they have to acquire them.

2.2 Correlation Terms for Tracked Ultrasound Sweeps

As observed by Housden et al., the correlation between two ultrasound frames depends on both their proximity and their orientation [Housden07]. Therefore, we introduce two correlation terms that we will use in the different steps of our ultrasound compounding pipeline.

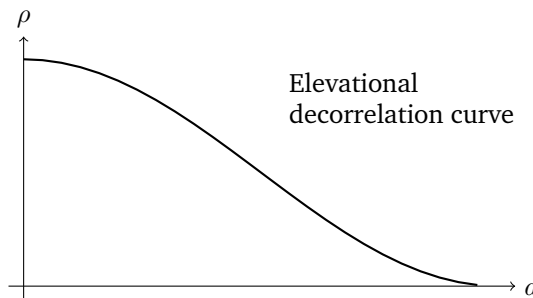


Fig. 2.2 Elevational decorrelation curve describing the distance between two adjacent ultrasound frames given their correlation ρ [Housden07, Chen97, Afsham14].

Technically, the elevational decorrelation curve describing the distance d of two frames given a correlation ρ is of non-linear form (cf. Fig. 2.2) and needs to be carefully calibrated to the used ultrasound transducer [Housden07, Chen97, Afsham14]. However, since we assume to have tracking information available, we do not need to solely rely on speckle decorrelation and can approximate the elevational speckle curve by a linear function, which allows for a generic formulation. For two tracked ultrasound frames i, j with centroids c_i, c_j , we consider their correlation to be zero if their Euclidean distance exceeds a threshold d_{\max} , while their correlation should be maximal if $c_i = c_j$. Therefore, we define

$$D(i, j) := \max \left(\frac{d_{\max} - \|c_i - c_j\|}{d_{\max}}, 0 \right), \quad (2.1)$$

which normalizes the correlation to the interval of $[0, 1]$. A value of 1mm for d_{\max} showed excellent results for all our experiments. While yielding comparable results for standard cases, this distance-based correlation term is not only simpler than the original Gaussian window formulation in [Schultezub14], but also a more robust generalization since it does also allow for non-homogeneous frame sampling rates.

We model the orientation-based correlation between two ultrasound frames by the cosine distance of their normals. Thus, for two tracked ultrasound frames i, j with normals n_i, n_j , we define the orientation-based correlation term as

$$O(i, j) := \max \left(1 - \frac{2}{\pi} \cdot \cos \left(\frac{n_i \cdot n_j}{\|n_i\| \|n_j\|} \right), 0 \right), \quad (2.2)$$

which is a simple extension of the Euclidean dot product formula, normalized to yield results in the interval of $[0, 1]$. In both terms, the maximum function avoids negative correlations.

2.3 Orientation-driven Inter-frame Registration of Ultrasound Sweeps

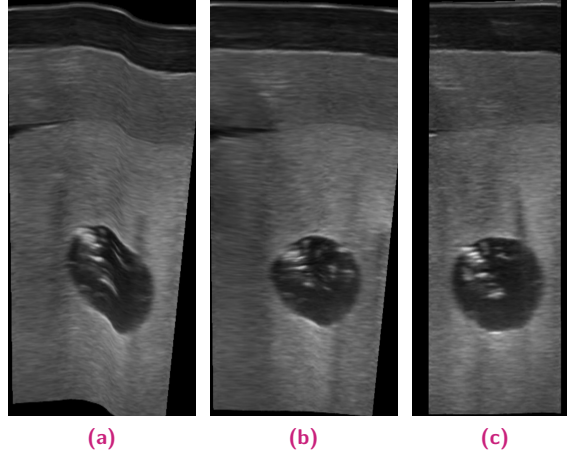


Fig. 2.3 Reconstruction of an **abdominal phantom scan with probe pressure changes**: (a) MPR through the compounded volume without applying our pressure compensation technique; (b) the same MPR through the compounded volume with pressure compensation applied. For comparison, (c) shows the same target acquired using constant probe pressure.

To correct for errors and inaccuracies in the tracking data (e.g. due to jitter, inaccurate calibration or patient movement), we use the above framework for performing an intensity-based inter-frame registration, similar to Treece et al. [Treece02]. Since the image changes are minimal for adjacent ultrasound frames in a sweep, a simple and thus real-time capable pixel-wise uphill search evaluating the SSD is sufficient for registering each ultrasound frame to its surrounding frames in terms of in-plane translation and in-plane rotation. To effectively compensate for registration drift, we regularize by registering each ultrasound frame to a window of N surrounding frames. Thus, for a given reference patch P and equally sized moving patch P' the windowed SSD (wSSD) is given by

$$\text{wSSD}_{P,P',N}(i) = \sum_{\substack{(p,p') \\ \in P \times P'}} \sum_{n=-N}^N C(i, i + n) \cdot (I_i(p) - I_{i+n}(p'))^2, \quad (2.3)$$

where i is the index of the reference frame and $I_i(p)$ denotes the image intensity of ultrasound frame i at the position p .

The central part in Eq. 2.3 is the correlation term $C(i, j)$, which describes the correlation between frames i and j and weights the surrounding frames' contribution to the similarity measure. As motivated in the previous section, the correlation between the two frames depends on both their proximity and their orientation to each other. Therefore, we define the $C(i, j)$ as

$$C(i, j) := D(i, j) \cdot O(i, j). \quad (2.4)$$

To compensate for probe pressure artifacts, we apply the above inter-frame registration technique not only to a single patch, but to a grid of independent patches of $10\text{mm} \times 10\text{mm}$ size. We make the simplified assumption that for our applications a deformation model is sufficient, which expects the deformation to be only in transducer direction. Therefore, we allow in-plane translations of the individual patches. After computing the transformation for each patch as above, we regularize the deformation field using a Gaussian convolution, which corresponds to one iteration of a fluid-type demons registration [Nielsen96, Thirion98, Zikic11] on the abovementioned grid. We compute the coarse inverse deformation field using fixed-point iteration [Chen08], which is eventually extended to pixel level using bilinear filtering during the compounding process. A exemplary result is displayed in Fig. 2.3.

2.4 An Information-fusion Approach to Ultrasound Compounding

Compounding ultrasound frames acquired from different viewpoints is non-trivial since ultrasound may show different intensities for the same anatomy if it is scanned from a different angle or at a different time. This is due to the complex ultrasound image formation being dependent on many different factors such as view angle, probe pressure, patient position and breathing cycle. Thus, tortuous acquisition sweeps are particularly challenging to reconstruct since their frames overlap. Traditional compounding schemes based on averaging or distance-based weighting fail in correctly reconstructing such regions as illustrated in Fig. 2.4. Since closer pixels are preferred over pixels being farther away, the compounded voxel intensity mainly depends on the ultrasound frame of highest proximity. If we now consider a neighbor voxel, the closest frame may have a completely different orientation and thus show different information (due to the view dependency of ultrasound). The resulting reconstructions exhibit a low image quality with significant discontinuities in the anatomy. Furthermore, unwanted stripe or pixel artifacts may arise as depicted in Fig. 2.5a.

Besides promoting artifacts and inhomogenities, distance-based weighting can also lead to incorrect reconstruction results since the distance of the frame to the voxel has no correlation with the amount of information present in this pixel (i.e. level of uncertainty/noise). For instance, it may ignore a pixel being farther away but having low uncertainty and instead prefer a high uncertainty pixel (i.e. noise) because it is closer to the voxel.

These two issues are the main motivation for our proposed orientation-driven ultrasound compounding technique. It tackles them by partitioning the ultrasound sweep into clusters of similar alignment and then using additional uncertainty information in a two-step fusion approach. We assume that for each ultrasound pixel with intensity I_i , we also have an

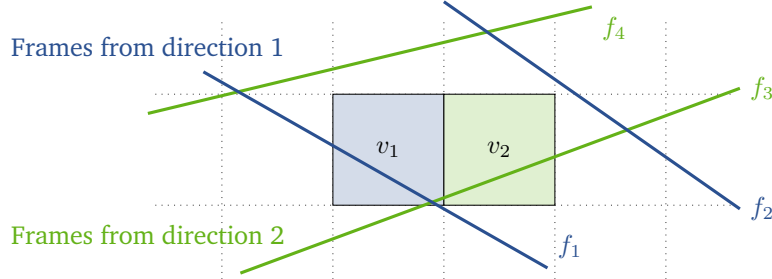


Fig. 2.4 Illustration of **artifacts occurring in distance-weighted compounded regions** where multiple ultrasound frames from different directions intersect. With traditional methods, voxel v_1 is mainly based on the information of frame f_1 while its neighbour voxel v_2 is mainly based on the information in frame f_3 . However, their intensities at this spatial location may significantly differ since the frames travel through different acoustic windows.

uncertainty value u_i that we will use for weighting the image intensities during compounding. While our method considers the generation of uncertainty information as black box and is thus independent from it, we use for our implementation the Confidence Maps as proposed by Karamalis et al. [Karamalis12]. Even though they model ultrasound physics only to a limited amount, their Confidence Maps can be interpreted as uncertainty information.

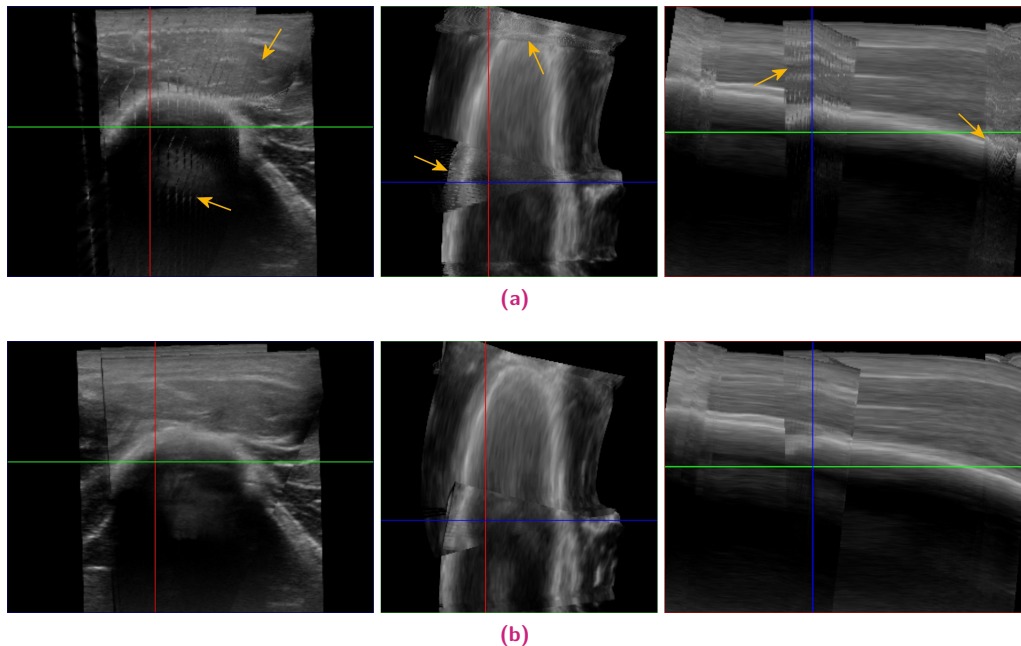


Fig. 2.5 Effect of the **orientation-driven clustering** of ultrasound frames: Both images show reconstructions of a tortuous sweep of upper arm ultrasound. (a) Traditional techniques with distance-only weighting show severe stripe artifacts (yellow arrows) in regions of overlapping frames. (b) Partitioning the sweep into clusters of homogeneous orientation and fusing the clusters based on uncertainty suppresses these artifacts almost entirely. Please mind that both volumes were compounded *without* applying our pressure compensation technique to highlight the beneficial effect of the orientation-driven clustering.

2.4.1 Clustering of Ultrasound Sweeps by Direction

As a first step, we perform a hierarchical clustering to identify tortuous sweep trajectories and regions of overlapping ultrasound frames. This partitions the ultrasound sweep trajectory into

parts where the frames have homogeneous orientation without requiring us to predefine the number of clusters. We apply an average group linkage algorithm on the previously defined orientation term $O(i, j)$ (cf. Eq. 2.2). This yields a set C of sub-sweeps meeting the usual restriction of being contiguous and uniformly oriented.

2.4.2 Compounding of each Cluster

A backward warping algorithm then compounds each cluster $c \in C$ into a 3D volume I_c applying our pressure compensation method as discussed in Section 2.3. Since the ultrasound frames of each cluster are guaranteed to have the same orientation and are thus travelling through the same acoustic window, we can safely assume the uncertainty distribution to be homogeneous within nearby frames. We compute the intensity for voxel x as

$$I_c(x) = \frac{\sum_{i \in S} I_i \cdot d_i^{-\mu}}{\sum_{i \in S} d_i^{-\mu}}, \quad (2.5)$$

where S is the set of frame pixels close to the compounded voxel x , d_i the Euclidean distance of pixel i to the compounded voxel, and $\mu > 1$ a smoothness parameter ensuring that $I_c(x)$ approximates the original data for $d_i \rightarrow 0$ [Shepard68]. Wein et al. showed that this inverse distance weighting scheme yields excellent results in terms of image quality [Wein06]. We use the same weighting to propagate the uncertainty to a separate 3D volume U_c :

$$U_c(x) = \frac{\sum_{i \in S} u_i \cdot d_i^{-\mu}}{\sum_{i \in S} d_i^{-\mu}}. \quad (2.6)$$

Thus, for each cluster $c \in C$ we end up with a compounded ultrasound intensity volume I_c and a compounded uncertainty volume U_c .

2.4.3 Uncertainty-based Fusion of the Compounded Clusters

In a final step, our method fuses the clusters together into the final 3D volume based on the propagated uncertainty values. We want the individual clusters $c \in C$ to contribute in an additive manner weighted by the propagated voxel uncertainties. Therefore, we compute the final intensity I at voxel x by

$$I(x) = \frac{\sum_{c \in C} (1 - U_c(x)) I_c(x)}{\sum_{c \in C} 1 - U_c(x)}. \quad (2.7)$$

Since we are acquiring a continuous sweep of ultrasound frames and apply a regularized inter-frame registration with active pressure compensation, we can safely assume that the individual clusters are well aligned. Hence, an additional 3D-3D registration is not needed.

2.5 Incremental Compounding System

For interventional usage, one does not only require short processing times, but also wants to support an interactive update of the compounded volume during the acquisition to allow for an additional refinement of selected regions. Therefore, we introduce *incremental ultrasound compounding* as a real-time capable extension of our orientation-driven compounding technique.

2.5.1 Incremental Compounding Pipeline

As illustrated in Fig. 2.1, our system receives a constant stream of incoming ultrasound frames. The regularized inter-frame registration (cf. Section 2.3) needs only a limited number of frames lookahead (i.e. size of the regularization window) and can hence be performed on-line requiring only a small number of frames to be buffered. We extend the orientation-driven clustering approach (cf. Section 2.4) to a partitioning into batches of ultrasound frames. In addition to starting new clusters when the correlation term exceeds the threshold, we also start new batches in a regular time interval (e.g. every second) to keep their size small.

Instead of reconstructing a separate volume for each batch, we use a single volume as accumulation buffer and adapt the above technique to an in-place algorithm. The reconstructed voxels of each cluster can be incrementally added to an accumulation buffer by rewriting Eq. 2.7 to a recurrence scheme. Given the accumulated compounded intensity I_{i-1} and accumulated compounded uncertainty U_{i-1} of the previous runs, and I_c, U_c of the current run, we define the new intensity I_i and uncertainty U_i as

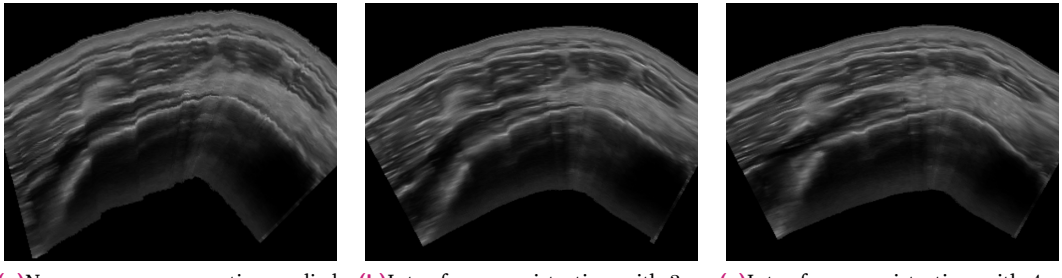
$$I_i = \frac{U_{i-1}I_{i-1} + (1 - U_c)I_c}{U_{i-1} + (1 - U_c)}, \quad (2.8)$$
$$U_i = U_{i-1} + (1 - U_c).$$

This transforms our technique into an on-line algorithm, significantly lowering the computational complexity and memory footprint and furthermore allowing for an interactive update of the visualization after each batch.

Apart from a slightly worse (but in our case neglectable) numerical stability, Eq. 2.7 and Eq. 2.8 yield the same reconstruction result. It should be noted that, with the incremental clustering, frames of the same orientation may end up in different clusters compared to the conventional formulation when they are separated by frames of different orientation. While technically this may alter the final result, we did not observe any qualitative differences in our experiments.

2.5.2 Real-time Implementation

The most time-consuming part of our reconstruction pipeline is the incremental compounding of each batch of ultrasound frames into the target volume. To yield high quality results, we employ a backward compounding technique where each voxel of the target volume is compared to each ultrasound frame to find contributing pixels (cf. Section 2.4.2). This process



(a) No pressure compensation applied. (b) Inter-frame registration with 3×4 patches yielding a patch size of $10\text{mm} \times 10.5\text{mm}$. (c) Inter-frame registration with 20×20 patches yielding a patch size of $7.5\text{mm} \times 2.1\text{mm}$.

Fig. 2.6 Multi-planar reconstructions of in-vivo acquisitions of the Infraspinatus muscle showing the **effectiveness of the pressure compensation**. Though the sweep was acquired by a professional sonographer trying to maintain constant probe pressure, the result of a traditional compounding technique (a) has an unsteady appearance and shows discontinuities throughout the different muscle layers. Applying our orientation-driven inter-frame registration and pressure compensation even on low resolution grid with $10\text{mm} \times 10.5\text{mm}$ patch size (b) yields a significant increase in image quality. Further increasing the resolution of the deformation field to $7.5\text{mm} \times 2.1\text{mm}$ patch size (c) yields only slight improvements.

can be parallelized heavily on voxel level. To exploit the new features of recent graphics hardware, we implemented the entire incremental compounding process on the GPU using OpenGL 4.3. To this end, we store the tracking information as well as other required data in Shader Storage Buffer Objects [**OpenGL43, SSBO**] and the image data of the ultrasound frames in 2D texture arrays to support hardware-accelerated interpolation during sampling. This allows us to yield highly interactive frame rates for the compounding process. This is further accelerated by exploiting that we do not need to traverse the voxels of the entire target volume but can restrict the reconstruction volume of each pass to the bounding box of the corresponding batch of ultrasound frames. Our information fusion approach exploiting uncertainty information ensures that the additional partitioning of the ultrasound sweep into batches does not impair the reconstruction quality.

2.6 Results and Evaluation

To evaluate our methods, we used an Acuson S2000™ ultrasound machine equipped with an Acuson 9L4 linear transducer and Ascension trakSTAR™ 2 electromagnetic tracking hardware. The system was calibrated using the method described in [**Wein08**], yielding an experimental calibration error of less than 2mm and 4 degrees. We acquired both phantom and in-vivo data of different anatomies where the in-vivo sweeps were acquired by a professional sonographer. All baseline results for comparison within this section were computed using our own implementation of a state-of-the-art backward compounding technique with inverse distance weighting as proposed by Wein et al. [**Wein06**].

2.6.1 Parameter Evaluation

To evaluate the effectiveness of our orientation-driven inter-frame registration and pressure compensation, and its dependency on parameters, we applied our technique to different

ultrasound sweeps of both phantom and in-vivo data. Figures 2.3 and 2.6 show representative results.

All experiments show a significant improvement in terms of image appearance and continuity of anatomy features when applying inter-frame registration, even with only minimal pressure changes present in the input data. In particular, the in-vivo scans show good results already with low resolution deformation fields, such as 3×4 patches for the Infraspinatus data set resulting in a patch size of roughly $10\text{mm} \times 10\text{mm}$. Increasing the deformation field resolution by decreasing the patch size yields only marginal improvements while increasing the computational burden (cf Fig. 2.6). Hence, in our implementation, we use a target patch size of $10\text{mm} \times 10\text{mm}$ as default setting.

2.6.2 Reconstruction Accuracy

To validate the physically correct reconstruction of anatomy, we acquired ultrasound sweeps of an abdominal phantom including a tumor target of spherical shape as depicted in Fig. 2.3. Since the target is positioned relatively close to the surface, it can be scanned from different directions and is prone to deformation. Therefore, this is a relevant scenario to evaluate our method. We computed 50 MPRs of arbitrary orientation through the target and compared the maximum diameter with reference measurements acquired from CT. The reconstructed ultrasound volume yielded an average target diameter of 14.63 ± 0.48 mm compared to 14.5 ± 0.84 mm in CT. This proves an excellent physical accuracy of our reconstruction method.

2.6.3 Reconstruction Quality

The qualitative effects of our inter-frame registration and pressure compensation technique can be observed in Fig. 2.3 and 2.6 showing the reconstructions of different ultrasound sweeps. The originally round target of the abdominal phantom (Fig. 2.3c) is severely deformed through probe pressure changes (Fig. 2.3a). Our pressure compensation technique is capable of mostly restoring the original anatomy (Fig. 2.3b). While the original shape is not perfectly restored, there is a clear improvement visible. Also Fig. 2.6 shows significant improvements in terms of continuity of anatomy when enabling our pressure compensation. Compared to [Treece02], there is still room for improvement. However, we want to emphasize that the implemented pressure compensation is of only complementary nature and the focus of this work is die orientation-driven clustering and compounding technique.

Fig. 2.5 demonstrates the effect of our clustering technique when reconstructing a twisted ultrasound sweep of a human arm exhibiting out-of-plane rotations of up to 35 degrees. Due to overlapping frames, the standard compounding in (a) shows artifacts at locations where the frames for neighboring voxels are acquired through different acoustic windows. The reconstruction in (b) removes such artifacts by using our clustering technique to avoid overlapping frames in a single cluster. Additionally, it exploits uncertainty information when fusing the clusters so that unreliable intensities do not bias the final result. Please note that, in order to highlight the effect of the clustering, these volumes were reconstructed without pressure compensation and thus show discontinuities in the anatomy.

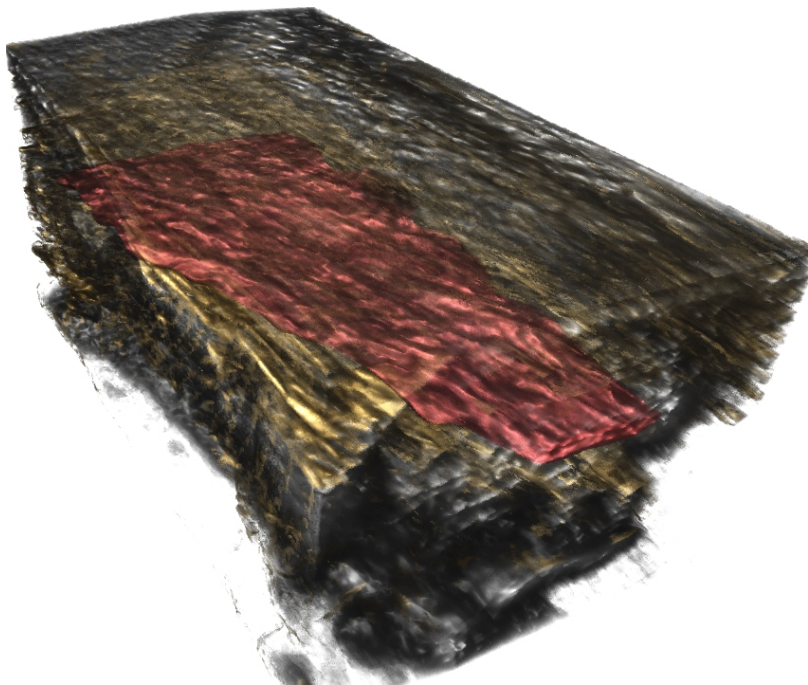


Fig. 2.7 3D visualization of an achilles tendon data set compounded with our technique. Due to the high curvature of the skin surface this is a challenging anatomy for sonography. Our clinical partners appreciate the high quality spatial reconstruction where possible lesions are easy to identify.

To further illustrate a clinical application, Fig. 2.7 shows a 3D visualization of an achilles tendon ultrasound volume acquired with our technique. Due to the high curvature of the surrounding skin surface, this is a challenging anatomy for ultrasound compounding. Our clinical partners highly appreciate the reconstruction quality where they can easily identify possible lesions in a spatial context.

To quantitatively evaluate the effectiveness of our orientation-driven compounding technique in terms of ensuring continuity of the anatomy and reducing artifacts in regions of overlapping ultrasound frames, we evaluate a local, scale-invariant entropy measure of the reconstructed sweeps. For every voxel we computed the intensity difference to the neighboring voxels and computed the mean and standard deviation over the entire volume. This measure penalizes high frequency intensity changes such as the mentioned stripe artifacts while preferring smooth and continuous reconstructions of the anatomy, which are desired for clinical and visualization purposes. To avoid biasing the result, we considered only the inner part of the volume and masked the outer faces of the sweep, as they naturally have a high entropy. The results as displayed in Table 2.1 show that our technique is sucessful in reducing the amount of reconstruction artifacts. While the entropy measures are not directly comparable between the data sets, all test data sets with a twisted probe trajectory show a significant drop in the mean difference and standard deviation. As reference, the first line shows the measure for a data set with a strictly linear sweep trajectory. Here, the drop in entropy turns out to be much lower.

For further quantitative evaluation we acquired pairs of overlapping sweeps with perpendicular main trajectory. After compounding the sweeps into separate 3D volumes using our methods, we applied a 3D-3D rigid registration using the tracking data as initialization. Expecting

Tab. 2.1 Quantification of the local entropy in compounded volumes in terms of mean intensity difference to neighboring voxels.

	Baseline [Wein06]	Our Technique
In-vivo leg / linear sweep	2.65 ± 2.42	2.49 ± 2.39
In-vivo arm / twisted sweep	4.59 ± 8.42	2.44 ± 4.62
In-vivo leg / twisted sweep	3.58 ± 5.82	2.34 ± 4.19
In-vivo carotid artery / twisted	7.2 ± 13.35	3.17 ± 8.58
In-vivo infraspinatus / twisted	4.17 ± 7.21	2.99 ± 6.17

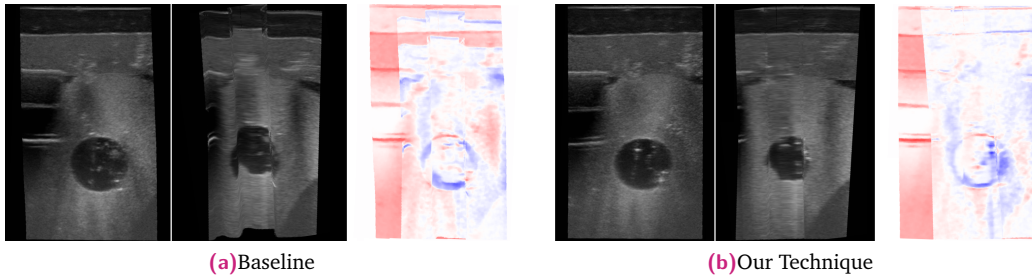


Fig. 2.8 **Illustration of our evaluation method:** First two images show the MPRs for each perpendicular sweep, the third one shows the color-coded absolute difference of their intensities after 3D-3D rigid registration. (a) traditional backward-compounding [Wein06] fails to align the different structures; (b) our technique yields alignment of all structures. The quantitative results are shown in Table 2.2.

our techniques to yield better matching volumes, we compared the differences of the two volumes in the overlapping region. With the average of the two volumes as expected result for a correct reconstruction, we quantify their difference in Normalized Cross-Correlation (NCC) and log-scale Signal to Noise Ratio (SNR_{dB}), for which define the signal as average of the volumes and the noise as RMS of the differences (Table 2.2).

The sweeps with pressure changes show a significant improvement in terms of increase in both NCC and SNR_{dB} when our technique is applied. Furthermore, when comparing constant pressure with pressure changes, our technique shows significantly less drop of the measures. The slight improvements for the sweeps acquired with constant pressure are mainly due to the inter-frame registration correcting for the tracking error. Since the sweeps are acquired with perpendicular trajectories and the volumes therefore show different interpretations of the underlying data, no algorithm yields a perfect match. Furthermore, the in-vivo sweeps are expected to have lower similarity since they show by far less homogeneous anatomy. Figure 2.8 shows the difference images for the second phantom sweep.

2.6.4 System Performance

For the evaluation of the system performance, we ran our implementation on a workstation with an Intel Core™ i7-4770 CPU and a nVidia GeForce™ GTX 670 GPU. We loaded recordings of different ultrasound acquisitions, streamed them into our incremental compounding pipeline

Tab. 2.2 NCC and log-scale SNR in the overlapping region after registering the two compounded volumes of two sweeps with perpendicular trajectories of the same anatomy.

	Baseline [Wein06]		Our technique	
	NCC	SNR _{dB}	NCC	SNR _{dB}
Phantom / constant pressure	0.90	19.39	0.94	23.16
Phantom / pressure changes	0.81	13.02	0.94	22.47
In-vivo leg / constant changes	0.72	9.21	0.76	11.69
In-vivo leg / pressure changes	0.67	8.53	0.75	11.03

and measured the time required for computing the final reconstructed volume at different resolutions.

Table 2.3 shows the timings for four exemplary data sets. The performance mainly depends on the number of frame pixels contributing to a single voxel (i.e. relationship between pixel size, voxel size and frame sampling rate) as well as the number of identified clusters (i.e. tortuosity of the sweep). The results show that for a clinically adequate resolution of 0.25 mm voxel size, our system has enough bandwidth to reconstruct ultrasound sweeps of very high framerate. Even high-quality reconstructions of 0.1 mm voxel size can be compounded at interactive frame rates.

2.7 Conclusion

In this work, we presented a novel orientation-driven approach featuring an incremental compounding scheme. We developed our methods with the aim to free clinicians from the restrictive scanning protocols of many of today's state of the art methods, which require the acquisition of linear probe trajectories and constant probe pressure. Our target application within this work was MSK ultrasound, where typical sweeps exhibit pressure changes, back-and forth and twisting motion. Therefore, we introduced a framework of two correlation terms to capture that the correlation of two frames in an ultrasound sweep depends on their proximity and orientation to each other. This framework is used to perform a complementary pressure compensation as well as a clustering of ultrasound frames by orientation to remove different kinds of artifacts. In the subsequent compounding process, we use an information fusion approach exploiting ultrasound Confidence Maps. This allows for more accurate reconstructions in regions where we have information from different acoustic windows, since intensities from uncertain regions do not bias intensity information from reliable regions. Finally, we presented an integrated system for incremental compounding that interactively fills the reconstructed volume while acquiring the sweep. This provides the clinician with direct feedback on the ongoing acquisition and allows for an interactive refinement of target regions.

We evaluated the different aspects of our technique using both phantom and in-vivo data, which was acquired by a professional sonographer. The results show that our methods accu-

Tab. 2.3 System performance of our incremental compounding technique at different target volume resolutions. The timings measure the compounding only (no generation of uncertainty information or visualization).

Voxel Size	Volume Size	Time	Speed
In-vivo arm			
0.5 mm	160 × 119 × 157	728 ms	687 fps
0.25 mm	320 × 237 × 313	1551 ms	322 fps
0.1 mm	800 × 591 × 781	13499 ms	37 fps
In-vivo leg			
0.5 mm	187 × 138 × 101	389 ms	620 fps
0.25 mm	373 × 276 × 214	906 ms	266 fps
0.1 mm	931 × 689 × 533	8433 ms	29 fps
In-vivo carotid artery			
0.5 mm	90 × 62 × 97	657 ms	743 fps
0.25 mm	179 × 124 × 194	735 ms	664 fps
0.1 mm	447 × 308 × 485	2569 ms	189 fps
In-vivo infraspinatus			
0.5 mm	114 × 104 × 178	609 ms	608 fps
0.25 mm	228 × 207 × 355	1135 ms	326 fps
0.1 mm	570 × 517 × 887	6761 ms	55 fps

rately reconstruct the original anatomy and yield superior results than traditional backward compounding methods in terms of image quality, continuity of the anatomy and presence of artifacts. Furthermore, the evaluation of our integrated incremental compounding system shows that the proposed system has enough bandwidth to reconstruct ultrasound sweeps with more than a hundred frames per second when using a clinically adequate target voxel size of 0.25mm. Even with high resolution volumes of 0.1mm voxel size, we still can yield interactive frame rates to update the compounded volume during the acquisition.

Hence, we see our orientation-driven approach as an important step towards providing clinicians with more freedom regarding 3D freehand ultrasound scanning protocols so that they can focus on which images the acquire instead of on how they have to acquire them. Current limitations of our work are mostly formed by the rather simple pressure compensation, which is not always capable of fully undoing all deformations. Therefore, as further work, we would like to merge more sophisticated pressure compensation techniques, such as [Treece02], into our orientation-driven framework.

t

Bibliography

- [1] John E Aldrich. “Basic physics of ultrasound imaging”. In: *Critical care medicine* 35.5 Suppl (2007), S131—7 (cit. on p. 5).
- [2] Rita Borgo, Johannes Kehrer, David H. S. Chung, et al. “Glyph-based Visualization: Foundations, Design Guidelines, Techniques and Applications”. In: *Eurographics 2013 - State of the Art Reports*. Ed. by M. Sbert and L. Szirmay-Kalos. The Eurographics Association, 2012 (cit. on p. 7).
- [3] Ralph Brecheisen, Anna Vilanova, Bram Platel, and Bart Ter Haar Romeny. “Parameter sensitivity visualization for DTI fiber tracking”. In: *Visualization and Computer Graphics, IEEE Transactions on* 15.6 (2009), pp. 1441–1448 (cit. on p. 4).
- [4] Ross Brown. “Animated Visual Vibrations As an Uncertainty Visualisation Technique”. In: *Proceedings of the 2Nd International Conference on Computer Graphics and Interactive Techniques in Australasia and South East Asia*. GRAPHITE ’04. Singapore: ACM, 2004, pp. 84–89 (cit. on p. 7).
- [5] John Butter, Thomas H Grant, Mari Egan, et al. “Does ultrasound training boost Year 1 medical student competence and confidence when learning abdominal examination?” In: *Medical Education* 41.9 (2007), pp. 843–848 (cit. on p. 6).
- [6] Paul K. J. Han, William M. P. Klein, and Neeraj K. Arora. “Varieties of Uncertainty in Health Care: A Conceptual Taxonomy”. In: *Medical Decision Making* 31.6 (2011), pp. 828–838. eprint: <http://mdm.sagepub.com/content/31/6/828.full.pdf+html> (cit. on p. 3).
- [7] L. Hao, C.G. Healey, and S.A. Bass. “Effective Visualization of Temporal Ensembles”. In: *Visualization and Computer Graphics, IEEE Transactions on* 22.1 (2016), pp. 787–796 (cit. on p. 4).
- [8] D. Kao, J.L. Dungan, and A. Pang. “Visualizing 2D probability distributions from EOS satellite image-derived data sets: a case study”. In: *Visualization, 2001. VIS ’01. Proceedings*. 2001, pp. 457–589 (cit. on p. 7).
- [9] G. Kindlmann and C.-F. Westin. “Diffusion Tensor Visualization with Glyph Packing”. In: *Visualization and Computer Graphics, IEEE Transactions on* 12.5 (2006), pp. 1329–1336 (cit. on p. 7).
- [10] Jason L Knudtson, Jonathan M Dort, Stephen D Helmer, and R Stephen Smith. “Surgeon-performed ultrasound for pneumothorax in the trauma suite”. In: *The Journal of trauma* 56.3 (2004), pp. 527–530 (cit. on p. 6).
- [11] C. Lundström, P. Ljung, A. Persson, and A. Ynnerman. “Uncertainty Visualization in Medical Volume Rendering Using Probabilistic Animation”. In: *Visualization and Computer Graphics, IEEE Transactions on* 13.6 (2007), pp. 1648–1655 (cit. on pp. 4, 7).
- [12] A.M. MacEachren, R.E. Roth, J. O’Brien, et al. “Visual Semiotics & Uncertainty Visualization: An Empirical Study”. In: *Visualization and Computer Graphics, IEEE Transactions on* 18.12 (2012), pp. 2496–2505 (cit. on pp. 6, 7, 10).
- [13] J. Alison Noble, Nassir Navab, and H. Becher. “Ultrasonic image analysis and image-guided interventions”. In: *Interface Focus* 1.4 (2011), pp. 673–685 (cit. on p. 5).

- [14] Henriette Obermaier, Kenneth Joy, et al. “Future challenges for ensemble visualization”. In: *Computer Graphics and Applications, IEEE* 34.3 (2014), pp. 8–11 (cit. on p. 4).
- [15] Tobias Pfaffelmoser, Matthias Reitinger, and Rüdiger Westermann. “Visualizing the positional and geometrical variability of isosurfaces in uncertain scalar fields”. In: *Computer Graphics Forum*. Vol. 30. 3. Wiley Online Library. 2011, pp. 951–960 (cit. on p. 4).
- [16] Konstantinos N Plataniotis and Anastasios N Venetsanopoulos. *Color image processing and applications*. Springer, 2000 (cit. on p. 9).
- [17] Kai Pöthkow and Hans-Christian Hege. “Positional uncertainty of isocontours: Condition analysis and probabilistic measures”. In: *Visualization and Computer Graphics, IEEE Transactions on* 17.10 (2011), pp. 1393–1406 (cit. on p. 4).
- [18] Jörg Stefan Praßni, Timo Ropinski, and Klaus Hinrichs. “Uncertainty-aware guided volume segmentation”. In: *Visualization and Computer Graphics, IEEE Transactions on* 16.6 (2010), pp. 1358–1365 (cit. on p. 5).
- [19] Marc Rautenhaus, Christian M Grams, Andreas Schäfler, and Rüdiger Westermann. “Visualization of 3D ensemble weather forecasts to predict uncertain warm conveyor belt situations”. In: *EGU General Assembly Conference Abstracts*. Vol. 17. 2015, p. 11908 (cit. on p. 4).
- [20] Christian Rieder, Thorben Kroeger, Christian Schumann, and Horst K Hahn. “GPU-based real-time approximation of the ablation zone for radiofrequency ablation”. In: *Visualization and Computer Graphics, IEEE Transactions on* 17.12 (2011), pp. 1812–1821 (cit. on p. 4).
- [21] Gordan Ristovski, Tobias Preusser, Horst K. Hahn, and Lars Linsen. “Uncertainty in medical visualization: Towards a taxonomy”. In: *Computers & Graphics* 39 (2014), pp. 60 –73 (cit. on p. 4).
- [22] J. Sanyal, Song Zhang, G. Bhattacharya, P. Amburn, and R.J. Moorhead. “A User Study to Compare Four Uncertainty Visualization Methods for 1D and 2D Datasets”. In: *Visualization and Computer Graphics, IEEE Transactions on* 15.6 (2009), pp. 1209–1218 (cit. on p. 7).
- [23] KA Scanlan. “Sonographic artifacts and their origins”. In: *AJR. American journal of roentgenology* 156.6 (1991), 1267—1272 (cit. on p. 5).
- [24] Christian Schulte zu Berge, Artur Grunau, Hossain Mahmud, and Nassir Navab. *CAMPVis – A Game Engine-inspired Research Framework for Medical Imaging and Visualization*. Tech. rep. Technische Universität München, 2014 (cit. on p. 11).
- [25] Junichi Tokuda, Gregory S. Fischer, Xenophon Papademetris, et al. “OpenIGTLink: an open network protocol for image-guided therapy environment”. In: *The International Journal of Medical Robotics and Computer Assisted Surgery* 5.4 (2009), pp. 423–434 (cit. on p. 11).

List of Figures

1.1	Uncertainty visualization of radio-frequency ablation zones as proposed by Rieder et al. [20].	4
1.2	Uncertainty visualization of segmentation algorithm results as proposed by Prassni et al. [18].	5
1.3	Kidney ultrasound using the liver as acoustic window with applied uncertainty visualization using chroma as visual variables (cf. Section 1.4). A slight repositioning of the transducer results in a considerable increase of confidence in image (b) compared to (a).	5
1.4	Schematic diagram of the different proposed uncertainty visualization schemes. Given the original B-mode ultrasound image I , we compute its Confidence Map CM and a Gaussian blurred version G_σ . The uncertainty map U is derived from CM by inverse linear mapping (cf. Equation 1.1). For the color overlay and the uncertainty mapping to chroma, we compute a derived uncertainty measure U' using a transfer function. Finally, the uncertainty information is fused into the original ultrasound image using one of the three visualization schemes.	8
1.5	Illustration of the color overlay mapping scheme. The high contrast yellow overlay allows for an [<i>clear investigation?</i>] of the signal loss effects in ultrasound.	9
1.6	Illustration of the chroma mapping scheme. Unreliable regions in the image are depicted with an orange overlay. Since the color transformation is applied in the perceptually uniform CIE L*C*h* color space, the perceived pixel intensity is maintained.	10
1.7	Illustration of the fuzziness mapping scheme. Unreliable regions in the image are blurred while reliable regions are sharpened through unsharp masking. Especially in video sequences this provides a very strong perceptual cue for uncertainty while at the same time maintaining the ultrasound image in its original gray scale color domain.	11
1.8	User study results on the educational value of our technique to ultrasound novices. Almost all test subjects appreciate the added uncertainty visualization and confirm that it helps them with understanding the ultrasound image formation process and getting a better understanding of uncertainty in B-mode imaging.	12
1.9	User study results on the perception and clinical value for ultrasound novices on a 5-point Likert scale. While there is no clear favorite visualization scheme, a bias towards the colorful mappings is present. Furthermore, some students said that the added information helps them with finding target anatomical structures faster.	13
1.10	Questionnaire results on expert sonographers' uncertainty perception . Each question was answered independently for the two different sequences. Therefore, there are 14 answers in total.	13

2.1	Schematic diagram of the proposed incremental compounding technique. We acquire a constant stream of tracked ultrasound frames and compute the per-pixel uncertainty for each frame. We furthermore, perform the on-line inter-frame registration and partition the stream into small batches of homogeneous orientation. Our incremental compounding then continuously compounds the batches into the accumulated ultrasound intensity and uncertainty volume. After each incremental compounding step the interactive visualization can be updated.	16
2.2	Elevational decorrelation curve describing the distance between two adjacent ultrasound frames given their correlation ρ [Housden07, Chen97, Afsham14].	18
2.3	Reconstruction of an abdominal phantom scan with probe pressure changes : (a) MPR through the compounded volume without applying our pressure compensation technique; (b) the same MPR through the compounded volume with pressure compensation applied. For comparison, (c) shows the same target acquired using constant probe pressure.	19
2.4	Illustration of artifacts occurring in distance-weighted compounded regions where multiple ultrasound frames from different directions intersect. With traditional methods, voxel v_1 is mainly based on the information of frame f_1 while its neighbour voxel v_2 is mainly based on the information in frame f_3 . However, their intensities at this spatial location may significantly differ since the frames travel through different acoustic windows.	21
2.5	Effect of the orientation-driven clustering of ultrasound frames: Both images show reconstructions of a tortuous sweep of upper arm ultrasound. (a) Traditional techniques with distance-only weighting show severe stripe artifacts (yellow arrows) in regions of overlapping frames. (b) Partitioning the sweep into clusters of homogeneous orientation and fusing the clusters based on uncertainty suppresses these artifacts almost entirely. Please mind that both volumes were compounded <i>without</i> applying our pressure compensation technique to highlight the beneficial effect of the orientation-driven clustering.	21
2.6	Multi-planar reconstructions of in-vivo acquisitions of the Infraspinatus muscle showing the effectiveness of the pressure compensation . Though the sweep was acquired by a professional sonographer trying to maintain constant probe pressure, the result of a traditional compounding technique (a) has an unsteady appearance and shows discontinuities throughout the different muscle layers. Applying our orientation-driven inter-frame registration and pressure compensation even on low resolution grid with $10\text{mm} \times 10.5\text{mm}$ patch size (b) yields a significant increase in image quality. Further increasing the resolution of the deformation field to $7.5\text{mm} \times 2.1\text{mm}$ patch size (c) yields only slight improvements.	24
2.7	3D visualization of an achilles tendon data set compounded with our technique. Due to the high curvature of the skin surface this is a challenging anatomy for sonography. Our clinical partners appreciate the high quality spatial reconstruction where possible lesions are easy to identify.	26
2.8	Illustration of our evaluation method: First two images show the MPRs for each perpendicular sweep, the third one shows the color-coded absolute difference of their intensities after 3D-3D rigid registration. (a) traditional backward-compounding [Wein06] fails to align the different structures; (b) our technique yields alignment of all structures. The quantitative results are shown in Table 2.2.	27

List of Tables

1.1	Quantitative evaluation results of our user study with ultrasound novices. The table shows the average time (<i>seconds</i>) required to optimize the view on target anatomies (aggregated results from 9 of the 13 users, since not all acquisitions were complete). With enabled uncertainty visualization, the users managed to decide faster when they had a good view on the target anatomy than with the plain B-mode image.	12
1.2	Results on expert sonographers evaluating the clinical value	14
2.1	Quantification of the local entropy in compounded volumes in terms of mean intensity difference to neighboring voxels.	27
2.2	NCC and log-scale SNR in the overlapping region after registering the two compounded volumes of two sweeps with perpendicular trajectories of the same anatomy.	28
2.3	System performance of our incremental compounding technique at different target volume resolutions. The timings measure the compounding only (no generation of uncertainty information or visualization).	29

Declaration

You can put your declaration here, to declare that you have completed your work solely and only with the help of the references you mentioned.

Garching bei München, November 16, 2015

Meng Ma

